ChemSusChem

Research Article
doi.org/10.1002/cssc.202300809

Chemistry
Europe
European Chemical
Societies Publishing

www.chemsuschem.org

Characterization and Comparative Study of Energy Efficient Mechanochemically Induced NASICON Sodium Solid Electrolyte Synthesis

Asma'u I. Gebi,[a, b] Oleksandr Dolokto,[a] Liuda Mereacre,[a] Udo Geckle,[a] Hannes Radinger,[a] Michael Knapp,[a] and Helmut Ehrenberg*[a]

In recent years, there is growing interest in solid-state electrolytes due to their many promising properties, making them key to the future of battery technology. This future depends among other things on easy processing technologies for the solid electrolyte. The sodium superionic conductor (NASICON) $Na_3Zr_2Si_2PO_{12}$ is a promising sodium solid electrolyte; however, reported methods of synthesis are time consuming. To this effect, attempt was made to develop a simple time efficient alternative processing route. Firstly, a comparative study between a new method and commonly reported methods was carried out to gain a clear insight into the mechanism of formation of sodium superionic conductors (NASICON). It was observed that through a careful selection of precursors, and the use of high-energy milling (HEM) the NASICON conversion process was enhanced and optimized, this reduces the processing time and required energy, opening up a new alternative route for synthesis. The obtained solid electrolyte was stable during Na cycling vs. Na-metal at 1 mA cm^{-1}, and a room temperature conductivity of 1.8 mS cm^{-1} was attained.

Introduction

The transition to clean renewable energy to reduce climate change requires efficient, competitive, reliable, and cost-effective large-scale energy storage systems. Since its commercialization, advancements in lithium-ion battery (LIBs) technology have led to high energy and power densities, cost reduction, and long cycle life, making it viable for applications such as high-performance portable devices and electric vehicles. Although it has satisfactory energy density levels, LIBs are not competitive large-scale electrochemical energy storage system (EES) candidates because of the high cost of critically important elements/lithium and uneven global distribution of these resources; hence, alternative technologies are rapidly developing. Sodium-ion batteries (SIBs) are a promising option due to sodium abundance, wide availability, low cost, and similar chemistry with lithium.[1,2]

[a] A.'u I. Gebi, Dr. O. Dolokto, L. Mereacre, U. Geckle, Dr. H. Radinger, Dr. M. Knapp, Prof. H. Ehrenberg
Institute for Applied Materials
Hermann-von-Helmholtz-Platz 1, 76344 Eggenstein-Leopoldshafen (Germany)
E-mail: Helmut.ehrenberg@kit.edu

[b] A.'u I. Gebi
Department of metallurgical and materials engineering
Ahmadu Bello University
Zaria Kaduna state (Nigeria)

Conventional SIBs like LIBs use flammable liquid electrolytes, raising safety concerns. Consequently, all-solid-state batteries (ASSBs) having a non-flammable ion-conducting solid-state electrolyte should overcome this challenge. A promising class of solid electrolytes with high ion mobility within a 3D framework, and good chemical and thermal stability are the sodium super ionic conductors (NASICON).[3] They have a general formula $AM_2(PO_4)_3$, where M can be a di-, tri-, tetra-, or pentavalent transition metal. Making it more attractive, their compositional diversity makes possible their application as cathode, anode, and solid electrolyte. This allows for an all-NASICON ASSB, as first reported by Lalere et al.[4]

The NASICON structure consists of a skeletal 3D array of corner-sharing MO_6 octahedra and PO_4 tetrahedra, which are stabilized by alkali ions, partially occupying interstitial sites.[5] The structure can be rhombohedral or monoclinic depending on the composition and temperature. Discovered by Hong in 1976, NASICON ($Na_{1+x}Zr_2Si_xP_{3-x}O_{12}$ ($0 \leq x \leq 3$)) has a rhombohedral structure, however, there is a distortion to the monoclinic phase in the range $1.8 \leq x \leq 2.2$. This modification has a high room temperature sodium-ion conductivity, and for this reason it is intensively investigated as a candidate for applications as solid electrolyte. Rhombohedral and monoclinic structures have two and three Na+ sites in one formula unit respectively. The Na+ sites comprise one Na1 (6b) and one Na2 (18e) site in the rhombohedral phase, the Na2 site splits further into one Na2 (4e) and one Na3 (8f) site in the monoclinic site, increasing its ion conduction pathways and ultimately its ionic conductivity in the standard $Na_3Zr_2Si_2PO_{12}$, where 75% of the Na sites are occupied.[6] Conduction occurs by jumping between Na1 to Na2 or Na3 sites, through triangles of oxygen atoms (known as bottlenecks) that have a common MO_6 octahedra and are separated by (Si/P)O_4 tetrahedra.[3]

ChemSusChem

Research Article
doi.org/10.1002/cssc.202300809

Chemistry Europe
European Chemical
Societies Publishing

Several synthesis methods such as conventional solid-state reaction (SSR),[5–10] sol-gel derivatives based,[3] hydrothermal,[11] co-precipitation,[12] and spark plasma sintering[13] have been reported in the literature for NASICON. The methods usually consist of several time-consuming steps (Figure 1); also there are slight variations in the reported conductivity values in the literature for the $Na_3Zr_2Si_2PO_{12}$ targeted composition. For instance, to synthesize $Na_3Zr_2Si_2PO_{12}$, Jolley et al.,[8] via SSR ball milled a mixture of precursors in isopropanol for 24 h, and then heated at 700 °C for 12 h. The mixture was further ball milled in isopropanol for 24 h, heated at 900 °C for 12 h, ball milled again in isopropanol for 24 h, and finally sintered at a range of temperatures between 1125 °C and 1200 °C, to attain a conductivity of 1.2 mS cm^{-1} which was correlated to a dense and uniform microstructure. Likewise, Jalalian et al.[9] via SSR used a six-step method and reported the best conductivity of 1.16 mS cm^{-1} attributed to homogenous grain growth and improved morphology. Hoping to obtain phase pure NASICON, Naqashi et al.[14] performed a five-step sol-gel based Pechini and a solution-assisted solid reaction synthesis and reached conductivities of 0.8 mS cm^{-1} and 1 mS cm^{-1}, respectively, due to higher densification and larger grains. Clearfield et al. obtained a conductivity of 0.66 mS cm^{-1} through a five-step hydrothermal synthesis method. Boilot and Selanie[12] used a co-precipitation method. Lee et al. using spark plasma sintering arrived at an ionic conductivity of 1.8 mS cm^{-1}. Clearly, for the same targeted $Na_3Zr_2Si_2PO_{12}$ composition, different process routes caused variations in the resulting ionic conductivity. Furthermore, the long milling times in the reported methods

make them energy intensive, affecting the total cost of synthesis. Therefore, due to the multiple steps and complicated way of synthesis, commercial NASICON material is expensive.

The future of solid-state electrolytes depends not only on their performance but also on cost-effective processing technologies. Therefore, continuous efforts are necessary to develop such methods as well as to understand how the different processing parameters affect the performance of the resulting material. Because every synthesis method has its specific processing conditions, for instance, different pre-sintering powder particle size distributions, compositions and morphologies are obtained from each method, which affect the final sintering in a different manner. Thus, several factors have been attributed to be responsible for the difference in conductivity. However, the origin of this differences is not sufficiently understood. In this study, the prospect of using high energy milling mechano-chemical synthesis (HEM), that allows intensive mixing, initiating reactive interactions, and reducing the number of processing steps and time for the synthesis of NASICON, was investigated. First, a comparative study of high-energy milling (HEM) with some already reported methods is reported to study the effects of processing route and identify the origin of these differences. Sufficient understanding of this is important for the future design and application of this important class of solid electrolytes. Phase evolution and purity, thermochemical, compositional, morphological, and electrochemical properties are characterized. The effect of large surface area precursors and different precursor combinations on early formation and conversion of $Na_3Zr_2Si_2PO_{12}$ NASICON
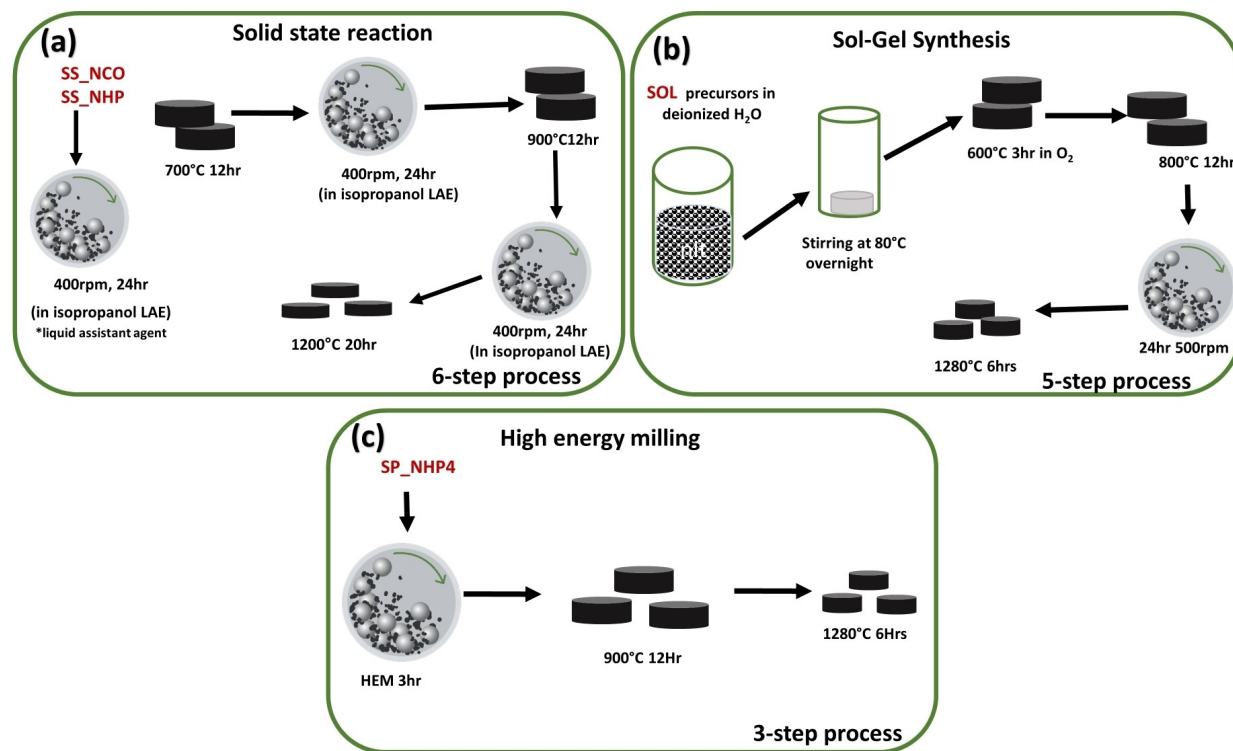
Figure 1. Flow outline of the processing steps of the a) 6-step solid state reaction b) 5-step sol-gel and c) high energy (HEM) mechano-chemical synthesis. Ref. [8]: Jolley et al. for the 6th step 1a) and Ref. [14]: Naqash et al. for the 5th step 1b).

ChemSusChem

Research Article
doi.org/10.1002/cssc.202300809

Chemistry Europe
European Chemical
Societies Publishing

was studied. Subsequently, the HEM synthesis route was optimized with respect to precursor combination, and the stability against sodium metal was investigated to evaluate the potential of the HEM NASICON.

Results and Discussion

Particle size distribution and surface area

The particle size distribution of powders (PSD) is a crucial factor for phase formation and microstructure evolution. The PSD analysis of samples prepared by different methods and precursor combinations is shown (Figure 2a), a log-normal PSD with maxima at approximately 1 μm&10 μm was observed in SS_NCO & SS_NHP, and 10 μm&60 μm SP_NH4 (see Experimental Section for detailed sample description). A bimodal distribution with 10 μm&60 μm average sizes was observed in SOL, which agrees with the morphology observed in SEM (Figure S1). From the results, the HEM after 3 h gave a particle size close to that obtained after 24 h of milling with the planetary ball mill. Such effect can be attributed to the higher mechanical energy of the shaker mill. Upon further investigation of the effects of precursor combinations on the PSD, it was observed (Figure 2) that although all combinations show a bi modal PSD, the sizes of SP_ZNO were much larger, averaging 100 μm&1500 μm against SP_NC, SP_NO, and SP_NOH, which averaged 10&60 μm. SP_ZNO showed high susceptibility to agglomeration. It might be related to the granular texture of the starting precursor and probable moisture absorption. Such property leads to having a higher tendency for its aggregation upon the start of milling, thus reducing milling efficiency. The result agrees with the powder morphology observed in the SEM images (Figure S1), which showed a range of similarly sized agglomerates. The Brunauer–Emmett–Teller (BET) surface areas are shown in Figure 2 b, d. In agreement with the trend observed in PSD, SS_NCO, SS_NHP, and SP_NH4 have a larger surface area. A similar trend was observed across the precursor combinations where SP_NC had the largest surface area, and SP_ZNO the smallest, indicating that both, processing routes and the precursor combination profoundly affect the PSD, surface area, and morphology. The PSDs and surface areas are in close agreement with what was observed by Jalalian et al.[9] and Naqashi et al.[14]
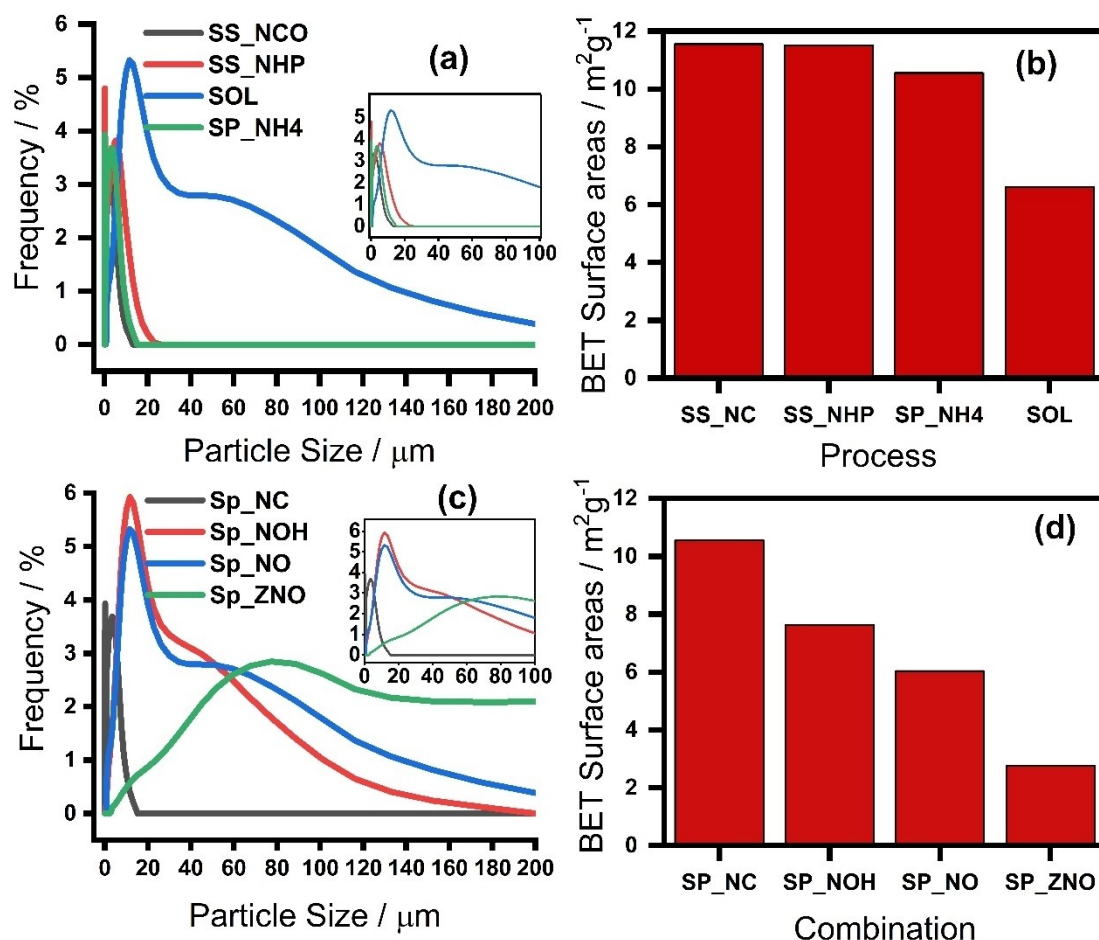
Figure 2. Particle size distribution (PSD) with corresponding surface areas for the processing routes; a,b) variation of particle size distribution and surface area with processing route; c,d) effect of precursor combination on the particle size distribution and surface area.

ChemSusChem

Research Article
doi.org/10.1002/cssc.202300809

Chemistry Europe
European Chemical
Societies Publishing

Phase transitions/evolution through the processing steps

To gain more insights into the different mechanisms/transitions that took place during the conversion of the starting precursor mixtures to the final product, samples from every step of each processing route were studied. The observations for the different processing routes are shown in Figures 3, 4, and 5. TG and DTA investigated the non-isothermal mass loss for the mixtures. The weight loss of the mixture during annealing occurs mainly at temperatures below 500 °C; this reflects reactants thermal decomposition/dehydration and oxidation reaction.[15] Three weight loss (5.2%) regions corresponding to the release of CO_2, chemisorbed water (H_2O), and NASICON formation were observed with increasing temperature for SS_NCO (Figure 3a). A corresponding broad peak with two endothermic humps at 820 °C and 1050 °C was observed on DSC of the same sample. The hump at 820 °C could be attributed to the conversion of low-temperature monoclinic ZrO_2 to tetragonal[16] and the onset of NASICON conversion. The hump at 1050 °C might be correlated to crystallization of NASICON.[17,18] Upon investigation of the SS_NCO XRD patterns (Figure 4e) at different processing steps, it was observed that the reflections after the first mixing in the planetary ball mill were mainly from precursor materials predominantly ZrO_2, implying that 24 h grinding with the mill

achieved size reduction and mixing but little or no initial reaction. After calcination at 700 °C for 12 h, ZrO_2 and intermediate $NaZr_2(PO_4)_3$ NASICON reflections were observed. Low intensity monoclinic NASICON $Na_3Zr_2Si_2PO_{12}$ (SG15, *C2/c*, PDF card: 01-070-0234) reflections with monoclinic ZrO_2 evolved after the second calcination at 900 °C for 12 h. A narrowing of the NASICON reflections due to increase in crystallinity and some monoclinic ZrO_2 secondary phase was observed after final sintering at 1200 °C.

The TGA of SS_NHP after the first 24 h of milling showed 5.79% weight loss in 3 regions between 25–200 °C, 200–300 °C, 400 °C–600 °C, and a steady region from 600 °C (Figure 3b).This might be ascribed to the decomposition of hydrate, phosphate, carbonate, and NASICON conversion and crystallization, respectively. Correspondingly, two dips at 190&277 °C and three peaks at 523 °C, 970 °C&1075 °C peaks were observed in DSC. This is in agreement with the observation from TGA and thus ascribed to similar phenomena. Furthermore, XRD (Figure 4b) after different steps reveals that the first 24 h of milling achieved mixing and size reduction without initial reaction. The reflections are mainly from the starting precursor. This might be related to the high thermodynamic stability of ZrO_2: it transforms from a low temperature monoclinic to an intermediate temperature tetragonal structure and participates in the final conversion to
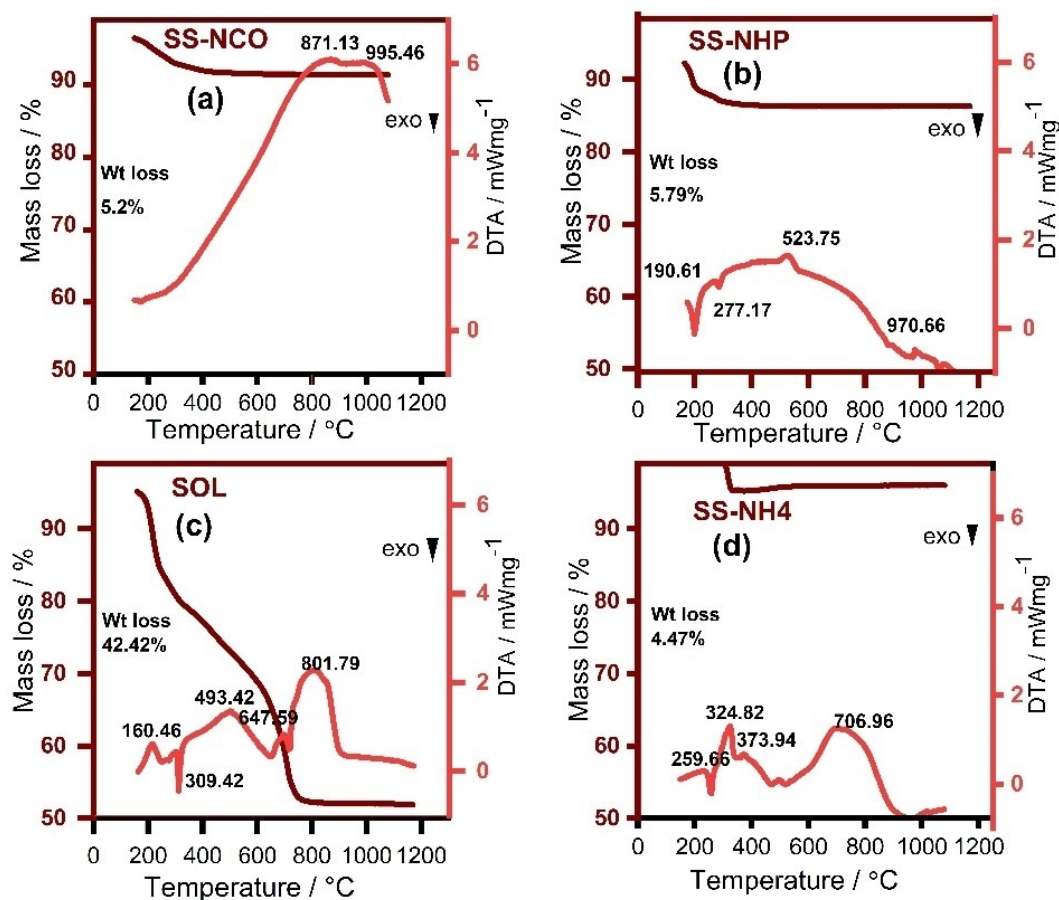
Figure 3. Temperature dependent transitions of the different processing routes. Corresponding TGA/DTA curves for a) SS_NCO, b)SS_NHP, c) SOL and d) SP_NH4 respectively, the brown curve and left axis indicate the thermogravimetric weight loss, while the right axis display the DTA.
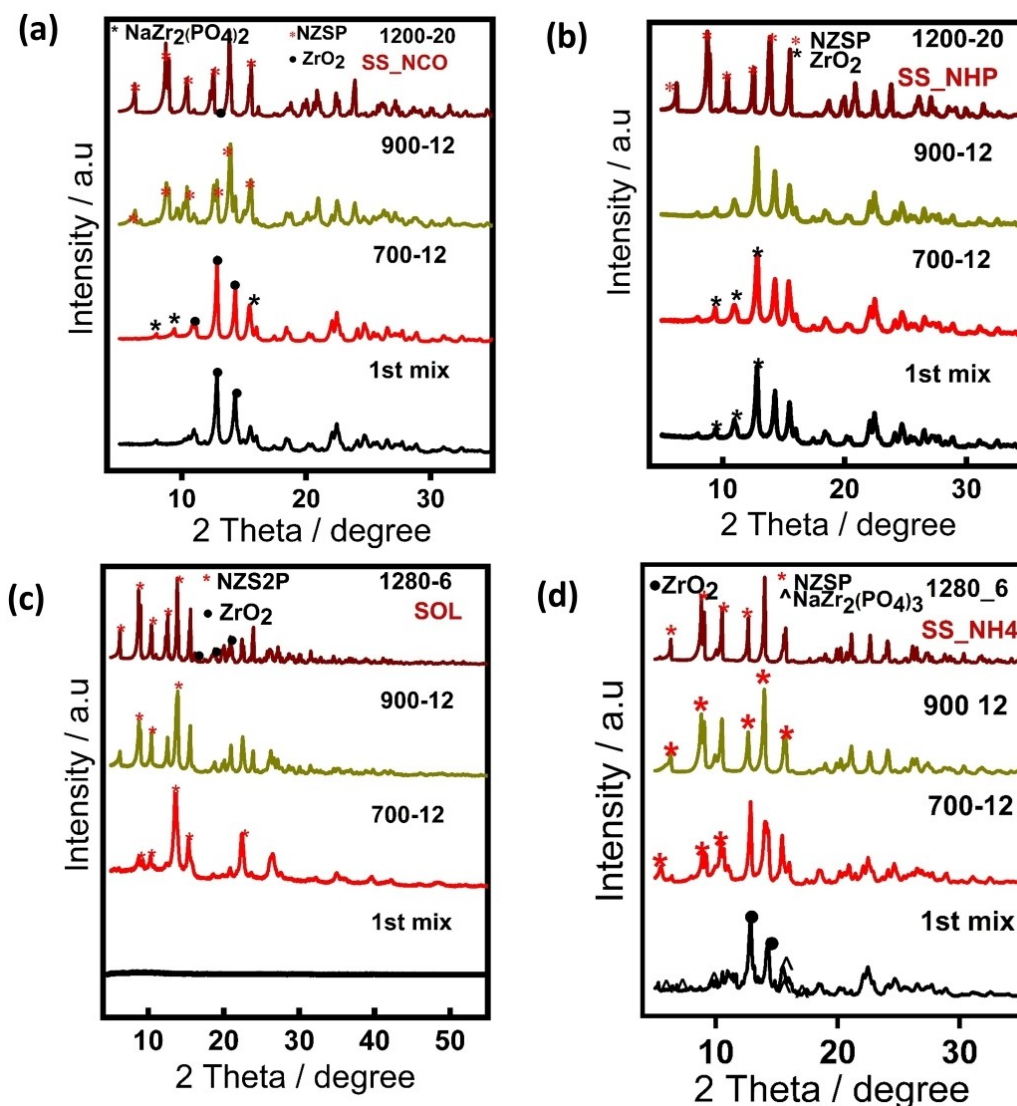
Figure 4. Room temperature XRD after each process step, for a) SS_NCO, b)SS_NHP, c) SOL and d) SP_NH4, respectively.

NASICON at high temperature only. Intermediate $Na_2Zr(PO_4)_2$ was observed after calcination at 700 °C for 12 h.[19,20] After 900 °C monoclinic NASICON was observed. Upon heating to 1200 °C a narrowing of reflections, an increase in intensity indicating increased crystallinity and a reduction in intensity of ZrO_2 phase was observed.

TGA of SOL revealed four main regions of thermal events (Figure 3c). The initial weight loss (42.42%) occurs between 25 °C and 170 °C with a dominant endothermic peak at 167 °C. It can be attributed to the loss of physiosorbed and chemisorbed water. Events of a greater magnitude follow with thermal peaks at 309 °C, 493 °C, and 717 °C corresponding to decomposition of, carbonates, and nitrates and NASICON formation[21] respectively, a continuous weight loss was observed until the residual mass was stabilized around 800 °C corresponding to the NASICON crystallization. The XRD (Figure 4c) of the initial gel showed no reflections. After calcination at 700 °C for 12 h, an

intermediate $NaZr_2(PO_4)_3$ phase appeared, and the sample crystallizes in the monoclinic structure after heating at 800 °C.

The TGA of SP_NH4 revealed four main regions (Figure 3d). The initial weight loss occurs between 100 °C–200 °C, 200 °C–300 °C, and 300 °C–400 °C. Correspondingly on the DTA dominant peak at 259.66 °C, 324.82 °C, 373.94 °C and 706.99 °C. Which can be ascribed to the loss of physisorbed water, decomposition of hydrates, carbonates water, and NASICON formation and crystallization, respectively. A gradual increase in weight from 400 °C to 500 °C was observed, this might be from the purging gas as no new phase that could be attributable to oxidation or reaction with the gas environment was observed within that temperature range on XRD. Subsequently, no further heat loss was observed. The XRD analysis (Figure 4d) of the sample after HEM, showed reflections of intermediate $NaZr_2(PO_4)_3$ phase and ZrO_2. Unlike for the sample from the planetary ball mill, monoclinic NASICON (SG15: $C2/c$, PDF code:01-070-0234) reflections begin to appear after calcination at 700 °C. The

sample crystallizes to the monoclinic structure after heating to 900 °C.

To further understand the structural evolution of NASICON in the different methods, HT_XRD was employed (shown in Figure 5). A similar trend was observed with DTA/DSC and room temperature XRD. After the first milling, SS_NCO and SS_NHP sample displayed broad diffraction peaks corresponding to monoclinic ZrO_2 (SG14: $P2_1/c$), no Na-containing phases were identified, likely due to the low scattering contrast of Na or its presence as an amorphous phase. Reflections of $Na_2Zr(PO_4)_2$ appeared around 700 °C, around 900 °C reflections from monoclinic NASICON were observed. The conversion kinetics was slow in both SS_NCO and SS_NHP, the intermediate phases and targeted NASICON phase appeared at high temperature in contrast to SP_NH4, where some intermediate phases were formed after HEM. This could be attributed to low mobility of ions and atoms in solids, a key factor that limits the rate of solid-state reactions. Consequently, high temperature and longer time is required to improve transport, reaction kinetics and complete the conversion of reactants to NASICON. This explains why a final sintering temperature of 1200 °C and 20 h time was reported in the compared method from literature to allow for complete conversion and crystallization.

An amorphous gel was obtained for SOL Increasing the temperature led to its decomposition and the onset temperature of the NASICON conversion was observed around 600 °C with the appearance of faint low and weak high angle −311, 131 and 421 reflections. The conversion was completed after
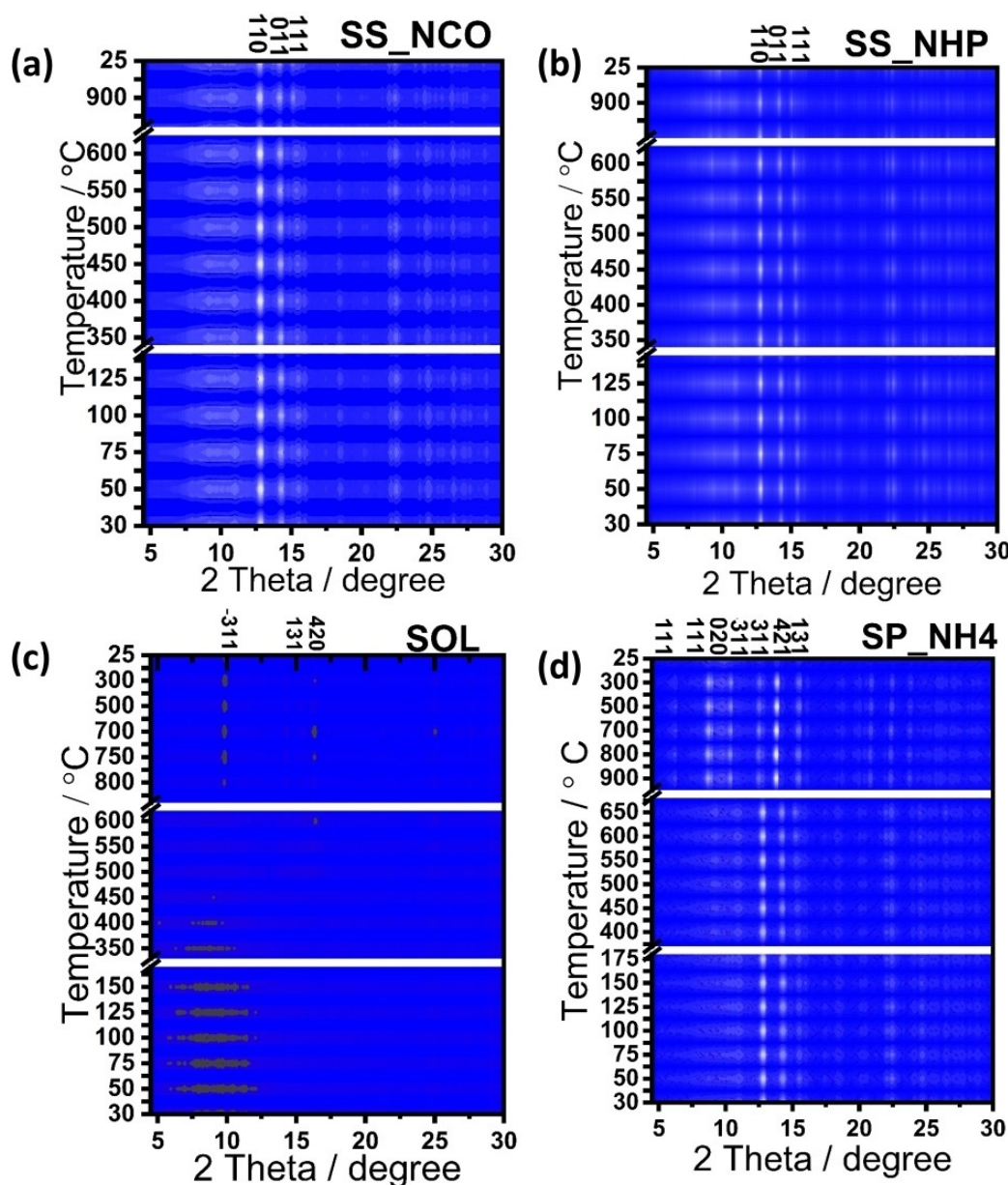
Figure 5. Temperature-dependent structural evolution of the different processing routes. High-temperature XRD for a) SS_NCO, b)SS_NHP, c) SOL and d) SP_NH4, respectively.

increasing the reported calcination time from 12 to 24 h (Figure 5c).

In the case of SP_NH4 (Figure 5d), broad diffraction peaks were identified after milling corresponding to coexistent crystalline phases such as: 1) a C2/c structured sodium zirconium phosphate (Na$_2$Zr(PO$_4$)$_2$), 2) a P2$_1$/c -structured ZrO$_2$, and 3) a C2/c phase typical of NASICON. Increasing the heat-treatment temperature from 900 °C to 1280 °C led to peak narrowing, indicating an increase in crystallinity commensurate with solid-state preparation of NASICON. To further understand the evolution of these phases in greater detail, multiphase Rietveld refinement was conducted on the patterns using the following phases: Na$_2$Zr(PO$_4$)$_2$, ZrO$_2$, Na$_3$Zr$_2$Si$_2$PO$_{12}$, etc (PDF Code: 189 807, 97 546, and 14 585, respectively). The phase ratios at different temperatures are given in Figure S3. Generally, for SP_NH4 where the fast kinetics was observed, the increase in temperature up to 900 °C and increasing the duration of heating led to an increase in the NASICON phase fraction and a decline in phases such as Na$_2$Zr(PO$_4$)$_2$ and ZrO$_2$.[20] The process proceeded according to equation (1) and (2), until a phase-pure NASICON sample was obtained.

Based on the detected phases, the decomposition reactions for SP_NH4 can be written using Equations (1) and (2):

$$Na_2O_2 + ZrO_2 + NaH_2PO_4 \cdot H_2O + SiO_2 \rightarrow$$
$$Na_{1+4x}Zr_{2-x}P_3O_{12} + Na_{1+4x} Zr_2Si_{2-x}O_8 + ZrO_2 + H_2O \quad (1)$$

$$Na_{1+4x}Zr_{2-x}P_3O_{12} + Na_{1+4x} Zr_2Si_{2-x}O_8 + ZrO_2 \rightarrow$$
$$Na_{1+x}Zr_2Si_xP_{3-x}O_{12} + ZrO_2 \quad (2)$$
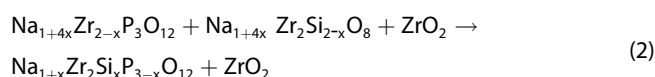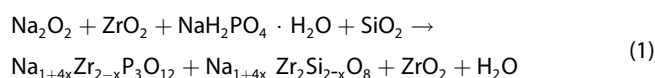
Clearly, compared to SS_NCO, SS_NHP, and SOL, the synthesis of SP_NH4 via a 3-h HEM, presents a simple alternative route for the synthesis of high purity NASICON. The effect of impact due to high-energy milling promotes early initiation of relevant intermediate reactions necessary for the formation of NASICON. Increase in temperature further increases the kinetics of the process due to increased mobility of ions and atoms. Phase pure NASICON was obtained via this route making it a good alternative for NASICON synthesis.

Variations in phase purity, lattice parameters and cell volume with processing

Depending on the thermal history, the samples crystallize in monoclinic or rhombohedral structure. In this study, all samples after final sintering exhibit the monoclinic symmetry. Rietveld refinement results based on the patterns of the different preparation methods are shown in Figure 6. Hong et al. described the structure of Na$_3$Zr$_2$Si$_2$PO$_{12}$ using the C2/c space group ($a = 15.586$ Å, $b = 9.0290$ Å, $c = 9.205$ Å, $\beta = 99.5°$, and $Z = 4$), the model was adopted for refinement. During refinement, the lattice parameters, profile parameters, atomic positions, atomic displacement parameter and occupancy were refined, as shown in Figure S3. The diffraction peaks of the sample were indexed, the lattice parameters, atomic displacement parameters, atomic coordinates and occupancies are presented in Tables S1–S4. As seen in Figure S4, SP_NH4 and SS_NHP had highest phase purity of 100% and 98.1%. SOL and SS_NCO have 9% and 5% monoclinic ZrO$_2$ as a secondary phase
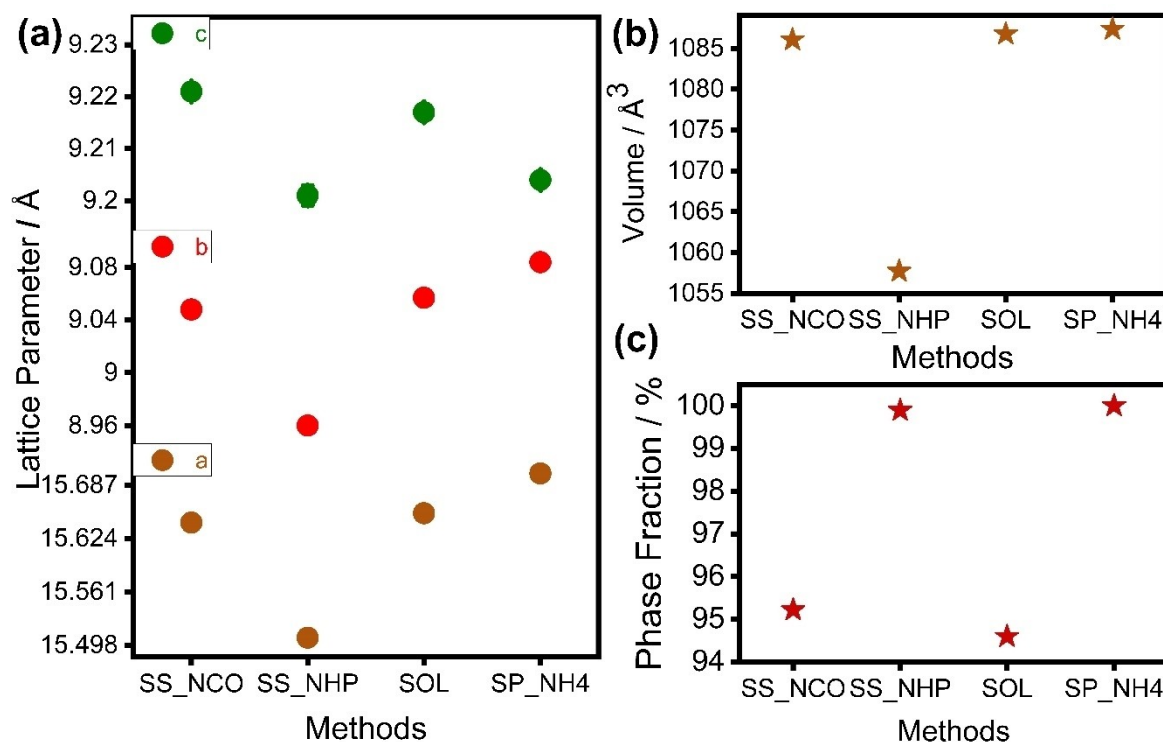
Figure 6. Variations in a) lattice parameter, b) unit cell volume, and c) NASICON phase fractions (ZrO$_2$ is the secondary phase) for the different methods.

ChemSusChem

Research Article
doi.org/10.1002/cssc.202300809

Chemistry
Europe
European Chemical
Societies Publishing

(Table S3 and S1). SS_NHP had smaller volume and lattice parameters compared to the other samples, this could be attributed to the smaller sodium and phosphorus occupancy observed. It could also be attributed to the effect of different sample preparation conditions on the unit cell parameters, as observed in an earlier study by Savinykh et al.[22]

Effect of processing route on the local microstructure

To investigate the effect of the processing routes on local microstructure Raman spectroscopy was used. The Raman band position and shape depends on the shared edges between octahedral/tetrahedral components and the average bond distances.[23] As such it is a useful tool for investigating short-range disorder in NASICON.[24] The vibrational modes of the NASICON lattice can be assigned to PO_4 tetrahedra internal and external modes, and to lattice modes including the motions of the metallic Zr^{3+} and Na^+ ions in their octahedral cage. The internal modes of the phosphate ions represent the symmetric v_s (PO) and antisymmetric degenerate v_d (PO) stretching of phosphorous to non-bridging oxygen, and the symmetric/antisymmetric degenerate δ_d (OPO) bendings. From Figure 7 the modes around 990 cm^{-1}, around 450 cm^{-1}, between 1050–1180 cm^{-1}, and 550–780 cm^{-1} are usually labelled v_1, v_2, v_3, and v_4, respectively. The PO_4 modes around 180 cm^{-1} and 85 cm^{-1} correspond to vibrational and translational motions of these tetrahedral groups.
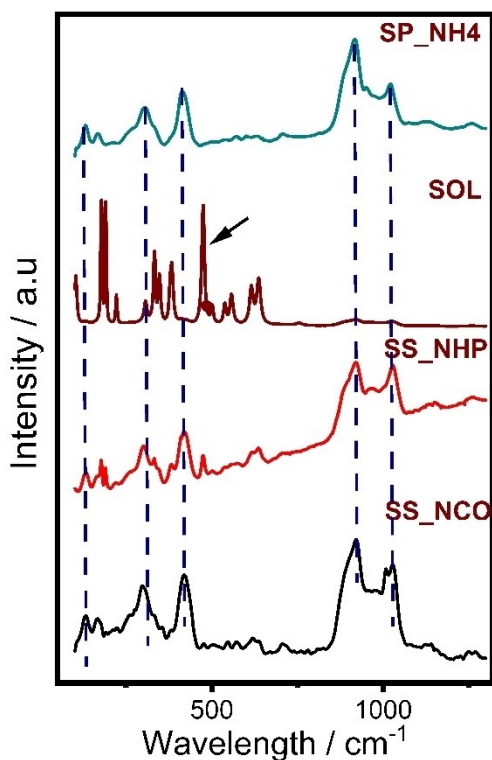
Figure 7. Raman Spectra showing bands for the different preparation methods (blue dashed lines show NASICON bands and the black arrow the ZrO_2 impurity bands).

For all processing routes, the spectrum of the monoclinic NASICON was observed with marked differences for SOL. Typical for monoclinic symmetry, the band in the range of 900–1000 cm^{-1}, which results from the stretching modes of PO_4 tetrahedra (v_1, v_2), is split into several modes as observed in all samples. The number of observed bands agrees well with the requirements of the prediction rule for the monoclinic symmetry.[25] 28, 25, 24, and 32 Raman band components (Figure S5) obtained by fitting of the data with CasaXPS were observed in SS_NCO, SS_NHP, SOL and SP_NH4, respectively. Reducing number of vibrational components and observing very broad bands indicate a short-range static disorder. According to Rietveld refinements SOL has the highest ZrO_2 impurity content, which has also a high Raman sensitivity as evidenced by the sharp monoclinic ZrO_2 bands at 180, 192, and 476 cm^{-1} and a shift in the Raman bands. Compared to the other processing routes, there is an increase in the width of the Raman components of the SOL. As well as a decrease in the number of the observed NASICON bands. This could be correlated to a static short-range disorder (SSRD) essentially associated with the partial occupation of the sodium sites and agrees with the observation of Barj et al.[25] Hence, even though both SP_NH4 and SOL enable a faster NASICON conversion, the thermodynamic stability of ZrO_2 in SOL is higher; it also has a high static disorder.

Effect of processing route on surface chemistry and structure

The chemical states (composition and bonding environment) of the composing elements are investigated by XPS. The survey spectrum (Figure S6) reveals the presence of the elements Na, Zr, P, Si, C, and O on the surface of the samples. Although the position of all peaks was corrected with respect to the C 1s signal at 285 eV, it can be seen, that all core level features of SS_NHP and SS_NH4 as well as SS_NCO and SOL align. These shifts might be related to internal charging of the structure which cannot be resolved by normalizing to an adsorbed carbonaceous species, whose influence on the underlying chemical states is debatable.[26] In the high-resolution detail spectra of Na 1s (Figure 8a), only one phase was identified for all samples between 1071.2 to 1071.5 eV, and no presence of carbonate phase in the $Na_3Zr_2Si_2PO_{12}$ was observed. However, the sodium concentration in the samples is highly different, ranging from 8 at% for SS_NHP up to 22 at% for SOL, see Table 1.

In contrast, all oxygen spectra (Figure 8b) show two overlapping features, from which the low binding energy peak (530.5 to 531.2 eV) can be assigned to the $(PO_4)^-$ and $(SiO_4)^-$ units in the NASICON lattice.[27] The high binding energy feature at 531.06 to 532.6 eV can be partially attributed to carbon-oxygen moieties adsorbed due to contact with the atmosphere and slightly differently bonded silicon and phosphorus complexes due to crystal defects and lattice mismatches. The latter assumption is supported by the relatively more intense secondary feature for SP_NH4, which reveals a higher amount of an additional silicon species (compare Figure 8e and Table 1).

ChemSusChem

Research Article
doi.org/10.1002/cssc.202300809

Chemistry
Europe
European Chemical
Societies Publishing
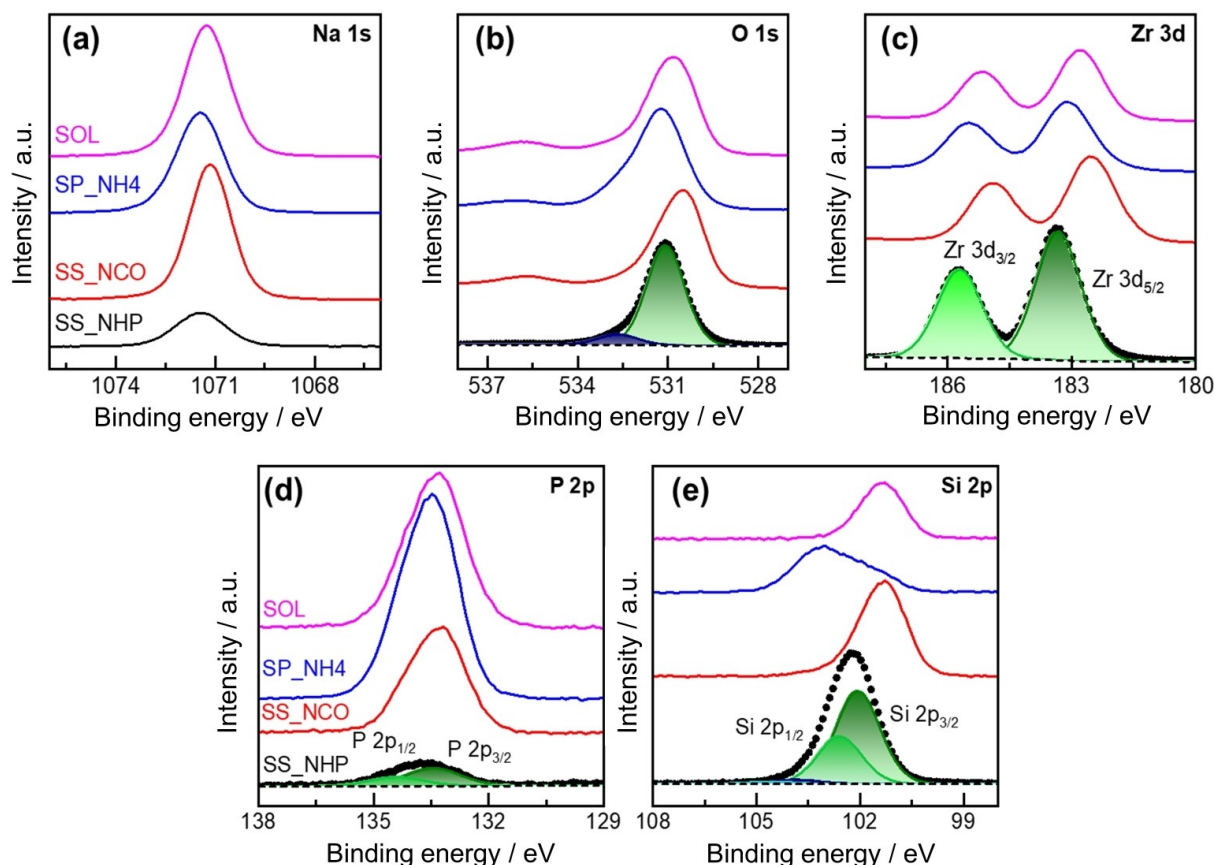
Figure 8. Surface chemical composition studied by X-ray photoelectron spectroscopy. Core level detail spectra of a) sodium Na 1s, b) oxygen O 1s, c) zirconium Zr 3d, d) phosphorus P 2p, and e) silicon Si 2p

Table 1. Quantification of the surface chemical composition revealed by XPS.

Sample	Na (at%)	O1 (at%)	O2 (at%)	Zr (at%)	P (at%)	Si1 (at%)	Si2 (at%)
SS_NHP	8	56	6	11	2	15.5	1.5
SS_NCO	21.5	51.5	5	6.5	6	9.5	1
SP_NH4	16.5	50	12	5	10	2	4.5
SOL	22	54	5.5	5	8	5	0.5

It is thus noted that all samples reveal an oxygen deficient (oxygen deficiency in NASICON was earlier suggested by Squaltritto et al.[28]) surface by only 4 and 5.5 at% for SP_NH4 and SOL, but up to 8 and 9.5 at% for SS_NHP and SS_NCO.

All zirconium-related signals (Figure 8c) arise from Zr^{4+} ions (282.5 to 283.4 eV) coordinated to the silicon and phosphorus oxides.[29] As Table 1 shows, the zirconium surface concentration for SS_NHP is almost doubled compared to the other samples. The inverse evolution is demonstrated for phosphorus (Figure 8d), which is only about 2 at% for this sample. In contrast, almost 90% of these sites in the crystal are occupied by silicon. As mentioned above, the secondary silicon phase which was found to a minor degree on all samples is more pronounced in SP_NH4 (Figure 8e). However, this must be related only to a different composition of the bulk from the surface, since no secondary Si-rich phase was observed by XRD.

There is also a variation between the bulk compositions measured with ICP-OES (Table S1) and the surface compositions quantified by XPS (Table 1). This can be related to the kinetics of the NASICON formation process as observed in both TGA/DTA and HT-XRD, which can lead to different decomposition and mass transport during the NASICON formation and having influence on transport of components to the surface.

Influence of processing route on micromorphology

The surface morphology and elemental composition was investigated by SEM/EDX. The micromorphology for the different processing routes is shown in Figure 9.

The images were obtained without additional polishing or thermal etching. For all samples, SEM showed that the powders

ChemSusChem

Research Article
doi.org/10.1002/cssc.202300809

Chemistry Europe
European Chemical
Societies Publishing
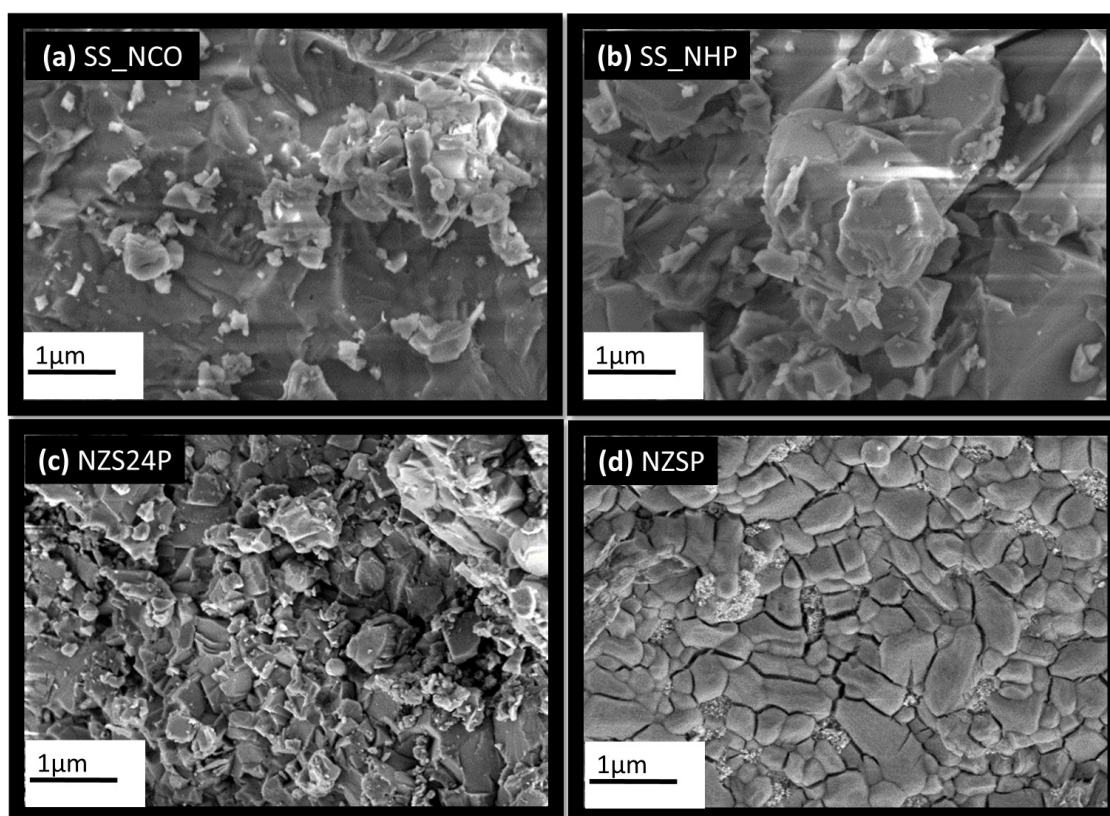
Figure 9. Morphologies investigated by scanning electron microscopy for, a) SS_NCO, b) SS_NHP, c) SOL and d) SP_NH4.

are compacted under high temperature sintering and the pellets become more densely packed compared to green pellets before sintering. Dense irregular faceted morphology was observed for both SS_NCO and SS_NHP (89 and 87% relative density respectively, measured geometrically and expressed relative to the theoretical value). SOL also shows an irregular faceted structure albeit with lower density (85%). SP_NH4 had near homogenous grains, however cleavage fracture occurred between the grains and the relative density was as low as 82%. SS_NCO, SS_NHP, and SOL. All had an embedded glassy/liquid phase. To further check stoichiometric proportion of all the constituents of NZSP, elemental mapping and quantification by EDX analysis were done. Figure S7 shows the Na, Si, P, Zr, and O distribution in the energy-dispersive X-ray (EDX) where all the elements are homogeneously distributed without any segregation.

Variations of ionic conductivities and activation energy with processing route

The conductivities were determined using AC electrochemical impedance spectroscopy (EIS) in the frequency range of 3 MHz to 1 Hz at room temperature. The resulting Nyquist plots, conductivities, and activation energies are illustrated in Figure 10. Typical impedance patterns, having a semicircle at the higher frequency side and a tail at the lower frequency side, are observed for all cases. The semicircle represents the bulk contribution, whereas the tail reflects the blocking electrode nature of Au against Na^+ ions. The conductivity of all samples with different sintering times is calculated using equation 3 (experimental section). Figure 10 shows that the conductivity of the samples is affected by the processing method. SS_NCO showed the highest ionic conductivity (0.2 mS cm^{-1}) in the series, SP_NH4 despite having high purity, delivers the lowest ionic conductivity (0.04 mS cm^{-1}). This might be attributed to the cleavage fractures observed between grains in the micro-morphology and low density. The presence of zirconia as a secondary phase and a much lower density for SOL also affects the conductivity (0.07 mS cm^{-1}). However, it is lower than the value reported in the literature (1 mS cm^{-1}). Generally, morphology and density greatly affect conductivity. It was observed that the relative density (expressed as a percentage of the geometric density relative to the theoretical) increases from SP_NH4 – SOL – SS_NHP – SS_NCO, with SS_NCO having the highest relative density 93%. Among all, the highest conductivity and lowest activation energy (0.2 mScm^{-1}, 0.32 eV) was achieved with the SS_NCO sample, because of its dense microstructure and large grain size (though embedded in an amorphous/ glassy phase). The fitted values of the equivalent circuit components are presented in Table 2. Nevertheless, the conductivity obtained for SP_NH4 is within the range of conductivities reported for the same material.

ChemSusChem

Research Article
doi.org/10.1002/cssc.202300809

Chemistry Europe
European Chemical
Societies Publishing
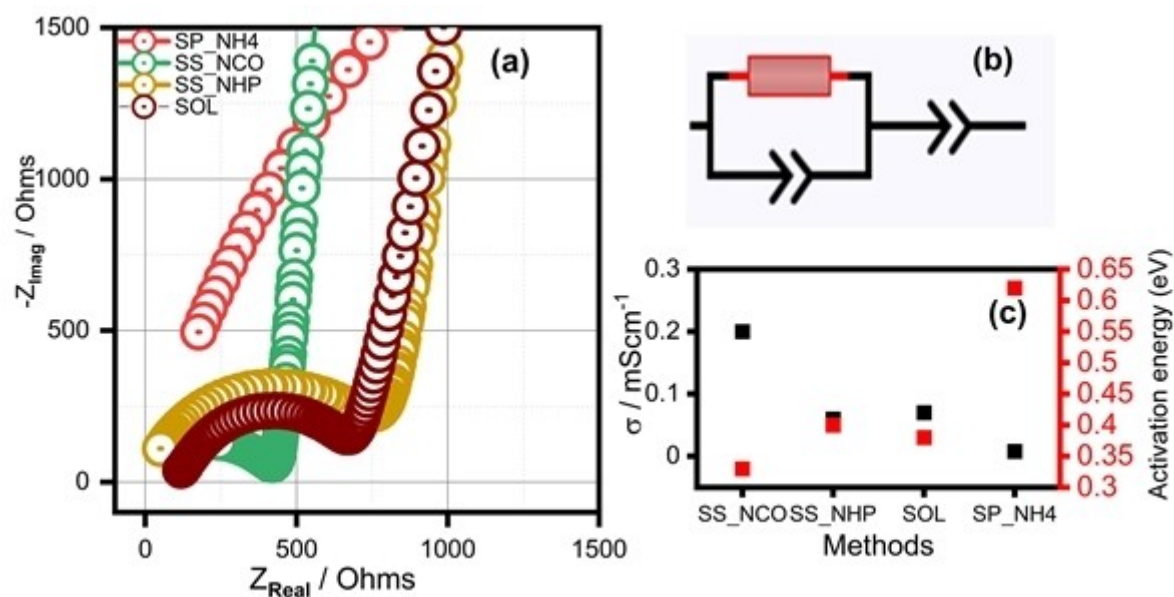
Figure 10. a) EIS spectra for the different methods, b) equivalent circuit used for fitting, c) ionic conductivities and activation energy for the different methods.

Table 2. Reference NASICON conductivities and conductivities from this study.

Sample	ionic conductivity [mS cm^{-1}]		Ref.
	measured	comparison	
SS_NCO	0.7	1 0.7	[14,30]
SS_NHP	0.6	1.55	[31]
SOL	0.4		
SP_NH4	0.04	1.2	[32]
SP_NC	1.8	1.13	[33]
SP_NOH	1.1	1.03	[17]
SP_NO	0.1	5	[36]
SP_ZNO	0.2	1.8, 0.2, 0.01	[13,34]

Influence of different precursors on HEM milling

Giving the potential of HEM at early NASICON formation and having observed the effect of morphology and density on the ionic conductivities as well as the fast kinetics of the NASICON conversion during HEM as revealed by DTA/DSC and XRD, an attempt was made to optimise the process; different precursor combinations as described in experimental section were used. Following the earlier observed influence of morphology on conductivity, the calcination temperature was increased from 900 °C to 1100 °C to eliminate trapped pores and increase density. The effects of the four sets of precursors on density, morphology, and ionic conductivities were analysed.

The XRD patterns in Figure 11, confirm what was earlier observed, the HEM milling initiated conversion reactions in all combinations, as evident by the formation of NaZr$_2$(PO$_4$)$_3$ after three h of milling in SP_NO, SP_NOH, and SP_NH4. SP_ZNO

formed NaNO$_3$ and an amorphous phase after the first milling. Upon calcination at 1100 °C, phase pure NASICON was obtained for SP_NC, other combinations gave some additional decomposition products. After sintering, dense, well-connected grains with average dimensions of about 1 μm were obtained for SP_NH4, and SP_NOH as seen in figure S10. SP_NC had a density of 94%, SP_NOH (90%), SP_NO (86%), and SP_ZNO (84%).

Increasing the calcination temperature increases the density of the samples. Figure 12 shows the ionic conductivities and activation energies for the obtained samples. Conductivities of samples from all combinations fall within the range of conductivities reported for samples, obtained by longer and more energy demanding preparation methods. SP_NC had the highest conductivity and lowest activation energy (1.8 mS cm^{-1}, 0.22 eV) this is close to the conductivity reported by Naqashi et al.[30] and Jolley et al.[31] as shown in Table 2. The observed differences could be attributed to microstructure.[9]

Cycling stability

Galvanostatic cycling performance of Na/SP_NC/Na (Figure 13) was tested at 1 mA cm^{-2} and 1 mAh cm^{-2} to investigate the cycling stability of the solid electrolyte with sodium anode at room temperature. A typical flat voltage plateau indicating good stability was obtained in the first eleven cycles. Subsequently, the cells show a slowly increasing slope in the voltage plateau during cycling in both directions (plating and stripping), likely due to polarization. Although an increase in overpotential was observed, it can be seen that this remained stable through the remaining cycling, which might be related to good conductivity and transference number of the solid electrolyte.[35] The slow increase in overpotential might also be attributed to the depletion and probable replenishment on the
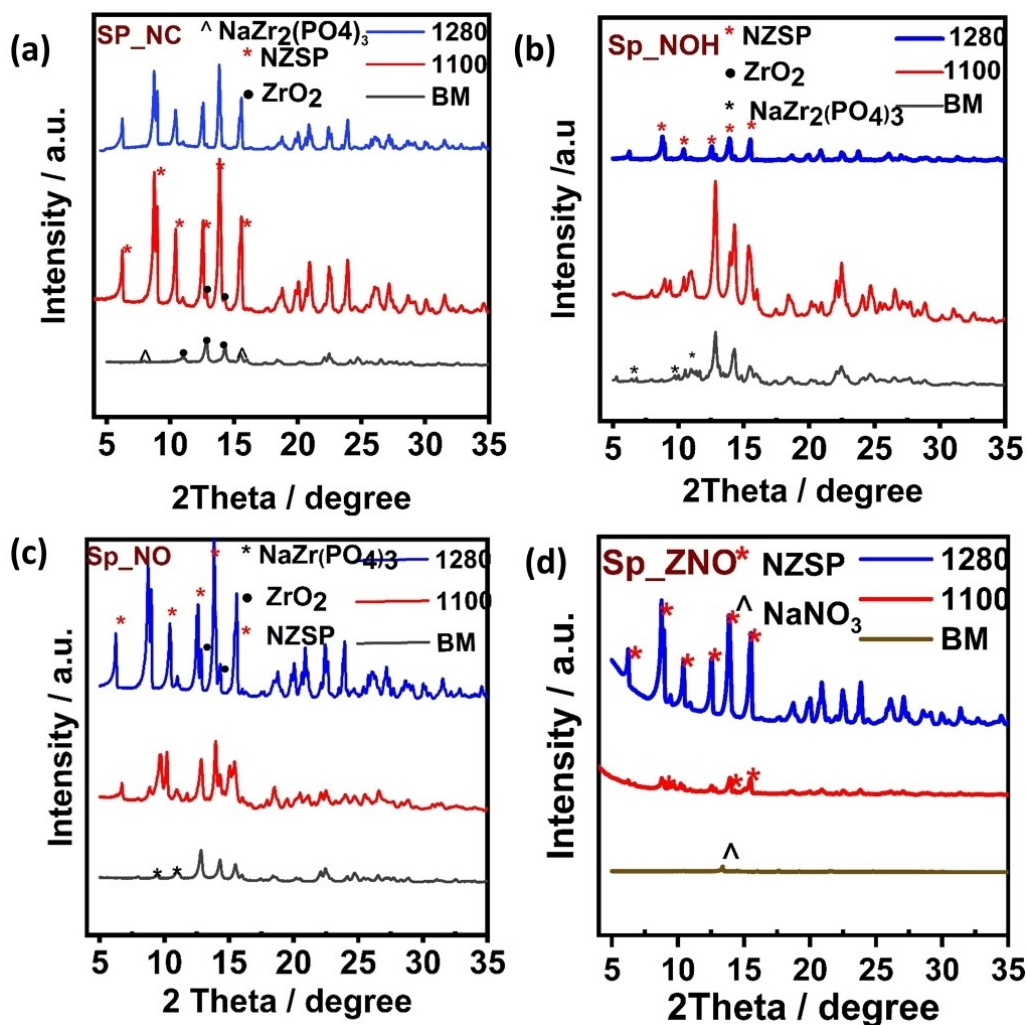
Figure 11. XRD illustrating phase evolution in a) SP_NO, b) SP_NOH, c) SP_ZNO and, d) SP_NC after different calcination temperatures and after ball milling (BM).
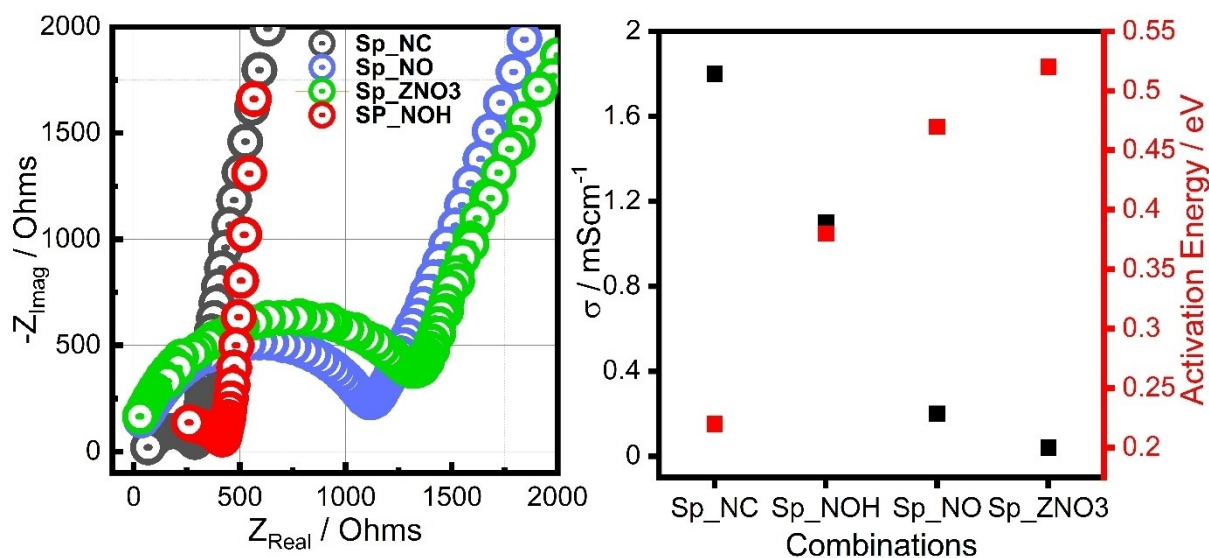
Figure 12. a) EIS spectra for the precursor combinations, b) Ionic conductivities and activation energy for the combinations.

ChemSusChem

Research Article
doi.org/10.1002/cssc.202300809

Chemistry Europe
European Chemical
Societies Publishing
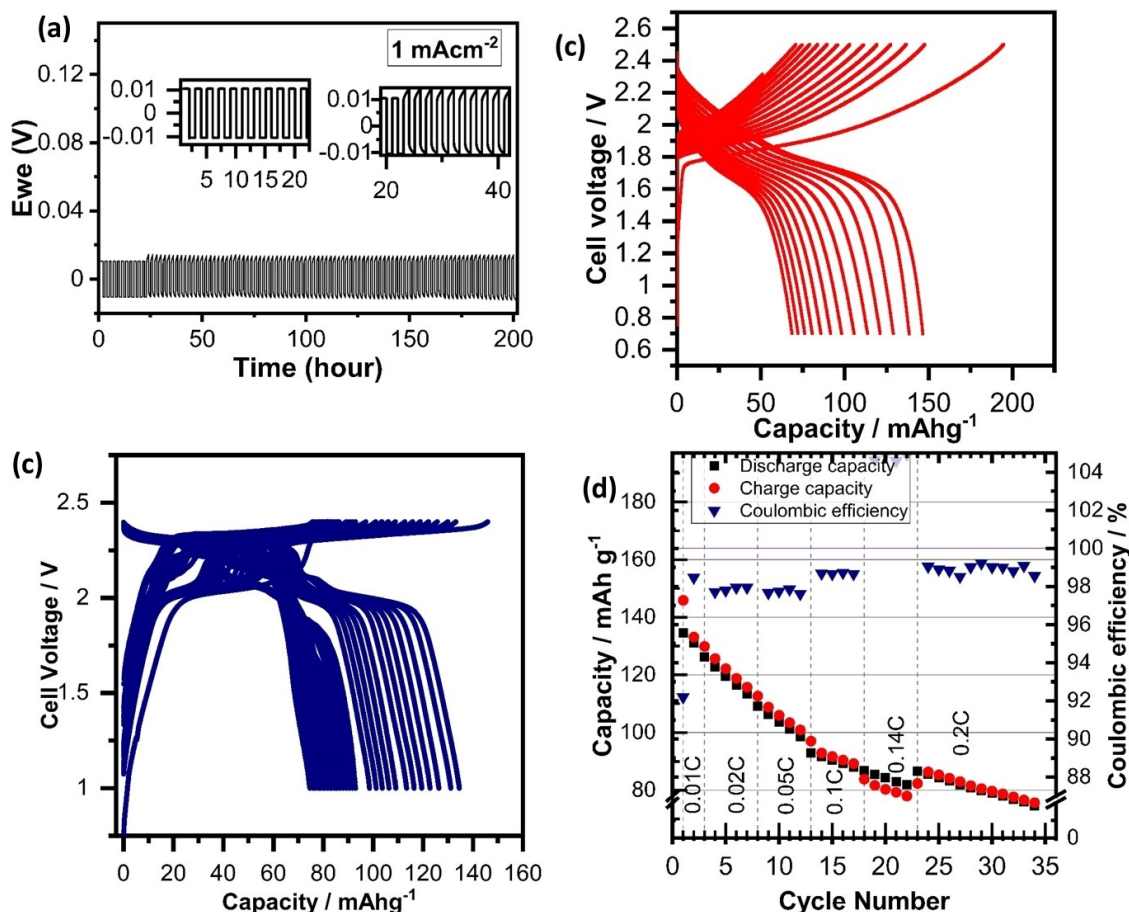
Figure 13. Striping and plating GCPL cycling of Na/NZSP/Na symmetric cells a) Galvanostatic charge discharge profile at 1 mA cm^{-2}_and 1 mAh cm^{-2} with zoomed in images in inset b) rate capability of Na/NZSP/NMO @ 60 °C c) rate capability of Na/NZSP/NMO-Au @ 60 °C d) capacity decay and coulombic efficiency profiles with different current densities.

surface during cycling, a similar phenomenon has been described by Lu et al.[35] as partly short circuit. The term 'partly short circuit' describes the primary stage of short circuit, during which the short circuit pauses or terminates subsequently. This could be due to the sodium penetrating partly, not through the whole bulk of the SE. Thus, the slight polarization voltage drop/increase represents the partial reduction of the bulk impedance. Because of the existence of bulk electrolyte impedance, the 'partly short circuit' is not regarded as a failure of a solid-state battery.[27] Ma et al.[36] in their study also observed a growth of dendrites on the edges of their NASICON solid electrode pellet and not through the bulk, which might also contribute to the partly short circuiting behaviour observed in this study.

Furthermore, the observed increase in potential might be attributed to grain boundaries, space charge and other defects. However, the low overpotential observed was in agreement with what was observed for the NASICON solid electrolyte in other studies.[37–39] For the HEM NASICON 1 mA cm^{-2} is the critical current density, This implies that the HEM NASICON solid electrolyte has good stability against Sodium and thus has promising capabilities with sodium anode.

Subsequently, the stability of the solid electrolyte in the presence of active material, a crucial factor for the practical application of sodium-ion batteries was investigated. The NZSP has been tested against NVP[4,40] FeS$_2$,[10] NTP.[37] Here, we examined the long-term stability of sodium manganese oxide (Na$_{0.67}$MnO$_2$) as a cathode material when cycled alongside the sodium zirconium phosphate (NZSP) solid electrolyte. This investigation was conducted at lower current densities than those typically used in symmetric sodium cells.

Cells with the configuration Na/NZSP/NMO, operating at an elevated temperature of 60 °C, displayed a significant capacity decay over prolonged cycling. This observation aligns with prior research findings, indicating that NMOs experience capacity fading due to structural degradation and dissolution of active materials during cycling.[41]

However, a significant improvement was attained when we coated a thin gold (Au) layer as a current collector onto the NMO cathode, creating the configuration Na/NZSP/NMO-Au @ 60 °C. In this case, we observed a notable reduction in the rate of capacity decay. This enhancement in stability can be attributed to the Au layer's ability to improve the electrical contact between the NMO cathode and the external circuit. By serving as a current collector, the Au layer mitigates the resistance within the system, reducing the potential for capacity fade and enhancing the overall performance of the battery.

While the energy density in the Na/NZSP/NMO-Au system remains relatively lower than that typically achieved with liquid electrolyte-based sodium-ion batteries, it is crucial to underscore the promising aspects of our solid electrolyte approach. Despite the lower energy density, this system offers competitive performance, especially when considering the good voltage and coulombic efficiencies achieved in our experiments. These efficiencies are indicative of the minimal loss of charge during cycling, a crucial characteristic for the practical use of sodium-ion batteries in various applications. The incorporation of a thin Au layer as a current collector on the NMO cathode significantly improves the stability of sodium-ion batteries when cycled with the NZSP solid electrolyte. While the energy density may be lower compared to typical liquid electrolyte systems, the performance and good efficiencies make this reliable electrolyte approach a viable option for sodium-ion battery technology.

Conclusions

A high energy mechanochemically induced synthesis was introduced as an alternative method to synthesize NASICON solid electrolyte. First, the method was compared to conventional solid state and sol-gel methods. It shows high potential for control, optimization and scale up in NASICON synthesis. Through a comparative study between the commonly reported preparation methods with the high energy ball milling (HEM), it was observed that by initiating reactions during the milling stage thus the use of high energy milling improved the NASICON conversion process. Correspondingly, processing time and steps were successfully reduced: from a 6-step in the conventional solid-state reaction to a 3-step process and from 24 h milling to 3 h with HEM. Formation of pure NASICON structure with HEM at 900 °C during the comparative analysis was attained. Pure Monoclinic NASICON phase was formed when the calcination temperature was increased to 1100 °C to improve densification. The high energy pre-treatment of HEM enhances the reactivity of ZrO_2 a common NASICON secondary phase and high purity NASICON phase was obtained after sintering at 1280 °C for 6 h. Furthermore, the NASICON obtained via HEM exhibits promising cycling stability (1 mA cm^{-2}) against sodium metal and NMO active material and has high potential for reproducibility. Hence, opening an alternative route for NASICON synthesis.

Experimental Section

$Na_3Zr_2Si_2PO_{12}$ (NZSP) was prepared for a comparative study by HEM and two other reported methods: solid-state (SS) and sol-gel (SOL). The solid-state reaction method reported by Jolley et al.,[8] and the sol-gel synthesis based on the method described by Naqashi et al.[14] (the reported calcination time was increased to obtain a pure phase at 800 °C), are compared with the method used in this study. In the solid-state reaction process, the stoichiometric mixtures underwent milling in a Fritsch planetary ball mill for 24 hours at 400 rpm in isopropanol. Subsequently, calcination was performed at 700 °C, followed by an additional milling step at 400 rpm for 24 hours in isopropanol. A subsequent annealing

process was conducted at 900 °C for 12 hours. Further milling at 400 rpm in isopropanol for 24 hours preceded the final stage, where pellets were sintered at 1200 °C for 20 hours, to obtain the solid electrolyte.

Conversely, for the sol-gel synthesis, the precursors were dissolved in distilled water until a clear solution was achieved. This solution underwent stirring and was heated at 80 °C overnight, leading to the formation of a dried gel. The dried gel was heated in oxygen at 600 °C for 3 hours, followed by treatment at 800 °C for 12 hours. Subsequent to this, the samples underwent milling at 500 rpm in isopropanol for 24 hours, finally pellets were sintered at 1280 °C for 6 hours.

As stated below, two precursor combinations for the solid-state reaction and one for sol-gel and HEM were used.

- Solid-state synthesis:

SS_NCO : $Na_2CO_3 + ZrO_2$ $_{(nano)}$ $+ NH_4H_2PO_4 +$

$SiO_{2(amorph.)}$ SS_NHP : $NaH_2PO_4 \cdot H_2O + ZrO_2$ $_{(nano)}$ $+ SiO_{2(amorph.)}$

- Sol-Gel Synthesis (SOL):

$NaNO_3 + ZrO(NO_3)_2 + NH_4H_2PO_4 + Si(OC_2H_5)_4$

- HEM (SP_NH4):

$Na_2O_2 + ZrO_{2(nano)} + NaH_2PO_4 \cdot H_2O + SiO_2$ $_{(Aerosil-90)}$
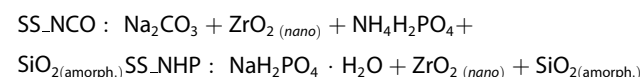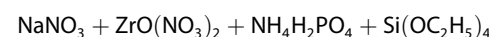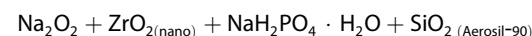
The precursors Na_2CO_3 (VWR chemicals), NaOH (Alfa Aesar), Na_2O_2 (Sigma Aldrich), ZrO_2 (15-25 nm Alfa Aesar), SiO_2 (AEROSIL® – fumed silica, 90 m^2 g^{-1} surface), $NaH_2PO_4 \cdot H_2O$ (Merck), $ZrO(NO_3)_2$ (Sigma Aldrich) and $SiO_{2(amorph)}$ (Sigma Aldrich) were used. The $SiO_{2(amorph)}$ is the common amorphous SiO_2, it has a smaller surface area compared to AEROSIL.

For the comparative study, stoichiometric mixtures of raw materials were taken through the steps outlined in Figure 1 for each processing route. A high-energy 8000 M SPEX mill was used for the method developed in this study and a Fritsch planetary ball mill for the reported solid-state synthesis.

In the developed method, the mixture of precursors with a selected molar ratio (total weight of ~1 g) was loaded in a 50 mL hardened-steel vial and ball milled for 3 h in the 8000 M SPEX mill. Steel balls of 20 g (2 large balls weighing 8 g each and 4 small balls weighing 1 g each) were used for ball milling. This was followed by the calcination and sintering step in air outlined in Figure 1.

For the optimisation of the HEM later on, the calcination temperature was increased from 900 °C to 1100 °C for 6 h. Sodium and zirconium sources were also changed to have different precursor combinations (SP_NH4 is renamed to SP_NO here because of the change in calcination temperature) as listed below:

SP_NCO : $Na_2CO_3 + ZrO_2 + SiO_{2(Aerosil-90)} + NaH_2PO_4.H_2O$

SP_NOH : $NaOH + ZrO_2 + SiO_{2(Aerosil-90)} + NaH_2PO_4.H_2O$

SP_NO : $Na_2O_2 + ZrO_2 + SiO_{2(Aerosil-90)} + NaH_2PO_4.H_2O$

SP_ZNO : $Na_2CO_3 + ZrO(NO_3)_2 + SiO_{2(Aerosil-90)} + NaH_2PO_4.H_2O$
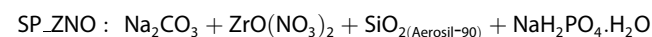
Nitrogen physical adsorption experiments were carried out to determine the surface areas of products, it was performed on a Quantachrome Quadrasorb evo instrument. The measurement parameters used were a pressure tolerance of 0.05 Torr, an equilibration time of 60 s, and an equilibrium time of 120 s. The Brunauer–Emmett–Teller (BET) specific surface area was determined from five data points between a relative pressure (p/p_0) of 0.1 and 0.25.

Laser diffraction spectroscopy was used to measure the particle size distribution (PSD) obtained using Horiba LA-950V2 analyser with ethanol as dispersing medium.

Differential Thermal Analysis (DTA coupled with a thermogravimetric analysis (TGA)) was used to study the thermochemical changes/phase transitions. It was carried out on an STA 449 C Jupiter instrument (NETZSCH, Germany), done in argon from room temperature to 1300°C with a constant heating rate of 5°C min^{-1} and an argon flow rate of 312.5 mL min^{-1}. The data were treated with NETZSCH Proteus thermal analysis software and Origin (peak analysis).

Room and high-temperature X-ray diffraction analyses (XRD) were used to study the structural evolution and phase purity. XRD patterns were collected using a STOE Stadi P powder diffractometer with Mo K$_{\alpha 1}$ radiation ($\lambda = 0.70932$ Å) with a linear Mythen2 detector module and a focusing Ge111 monochromator from 4 to 70 degree of 2θ. The data collection time was 5 h for each diffractogram at room temperature and 2 h for each at elevated temperature in HT_XRD. Rietveld refinement was applied using the XRD data to determine the lattice parameters and phase fractions of the obtained material using the Fullprof software package.[42]

Raman spectroscopy was used to study vibrational properties, performed with a LabRAM HR evolution spectrometer (HORIBA Scientific) using a 100× magnification objective and an excitation wavelength of 632.81 nm, using a 600 g mm^{-1} grating. The data were acquired at exposure times of 10 s with 15 accumulations over the wavenumber range from 100 to 1300 cm^{-1}.

Scanning electron microscopy (SEM) and Energy Dispersive X-ray Spectroscopy (EDX) was used to study morphology and elemental composition. Images were recorded on a Zeiss Merlin microscope using 5 kV and 30 kV acceleration voltages, respectively.

X-ray Photoelectron Spectroscopy (XPS) was used to determine the surface chemical composition of the samples. It was performed using a K-alpha$^+$ spectrometer (Thermo Fisher Scientific) with monochromatic Al-K$_\alpha$ radiation ($\lambda = 1486.6$ eV), and a spot size of ∼400 μm. Survey spectra were recorded with a pass energy of 200 eV, detail spectra with 50 eV. The Thermo Avantage software was used for data acquisition and spectra deconvolution, determining a Shirley background with the implemented smart background function. All spectra were binding energy corrected using the C 1s signal at 285 eV. Normalization of the intensity was achieved using the most intense oxygen O 1s signal for all core level data.

Electrochemical impedance spectroscopy (EIS) was used to estimate ionic conductivities. The ionic-conducting, semi-conducting, mixed-conducting, or dielectric behaviour and the dynamics of bound and mobile charge in the bulk and interfaces can be studied. Two-electrode EIS measurements are typical as they are experimentally simple and can be applied to a material, cell, or pack straightforwardly without modification (Kramers-Kronig relation was used for data validation). EIS of a 2-electrode cell using symmetric Au ion-blocking electrodes was used to extract the ionic conductivity (σ_{ion}) of the solid electrolyte, given by:

$$\sigma_{ion} = \frac{l}{R_{total}\ A} \tag{3}$$

Where R_{total} is the total resistance of the electrolyte sample which is obtained by fitting the impedance data with the equivalent circuit in Figure 10b, l is the sample thickness and A is the area. Measurement was done on Au sputtered samples with pellet geometry: 120 mg weight, 1 mm average thickness, 8 mm diameter and was performed on a VSP-300 Biologic in the frequency range of 3 MHz to 1 Hz, 3 samples were measured for each set of condition. Relaxis software was used for data fitting and conductivity was calculated from formula 1.

Galvanostatic coulometry with potential limitations (GCPL) was employed to measure the cycling stability. Symmetric cells were made by placing sodium electrodes on each side of the pellets, the sandwich was placed in an 8 mm diameter cell made of PEEK and a force of 3 kN was applied with a torque screw. 3 samples were measured to ensure data reproducibility. To study stability against Na, Na/NZSP/Na symmetric cells were cycled on a VMP potentiostat at 1 mAcm^{-2} current density. To study stability against active material all-solid state half cells were built with Na$_{0.67}$MnO$_2$ (NMO). To prepare the cathode of an all-solid-state Na/NZSP/NMO cell, the active material NMO was mixed with carbon black, PAN, and NaPF$_6$ (65:10:15:10 by weight) and ground in a mortar. The mixture was then dispersed in DMF at 50°C and stirred overnight. The obtained slurry was spread evenly on a carbon coated aluminium foil to produce an electrode film with an active material loading of around 2 mg cm^{-2}, which was dried at 60°C for 10 h under vacuum. Cells were fabricated in an argon-filled glove box with sodium foil as the anode. For the Na/NZSP/NMO-Au the slurry was cast on the pellet to a desired loading and the pellet was dried in vacuum at 60°C and Au was coated on the cathode side of the pellet. The cycling was done on a VSP potentiostat.

Acknowledgements

Conflict of Interests

The authors declare no conflict of interest.

Data Availability Statement

The data that support the findings of this study are available from the corresponding author upon reasonable request.

[1] Y. Deng, C. Eames, L. H. B. Nguyen, O. Pecher, K. J. Griffith, M. Courty, B. Fleutot, J. N. Chotard, C. P. Grey, M. S. Islam, C Masquelier, *Chem. Mater.* **2018**, *30*, 2618–2630.

[2] M. Chen, W. Hua, J. Xiao, D. Cortie, W. Chen, E. Wang, Z. Hu, Q. Gu, X. Wang, S. Indris, S. L. Chou, S. X. Dou, *Nat. Commun.* **2019**, *10*, 1480.

[3] M. Guin . vol. 373. RWTH Aachen Repository. https://juser.fz-juelich.de/record/830267/files/Energie_Umwelt_373.pdf.

[4] F. Lalère, J. B. Leriche, M. Courty, S. Boulineau, V. Viallet, C. Masquelier, V. Seznec, *J. Power Sources* **2014**, *247*, 975–980.

[5] H. Y. Hong, *Mat. Res. Bull.* **1976**, *11*, 173–182.

[6] H. Park, K. Jung, M. Nezafati, C. S. Kim, B. Kang, *ACS Appl. Mater. Interfaces* **2016**, *8*, 27814–27824.

[7] T. Takahashi, K. Kuwabara, M. Shibata, *Solid State Ionics* **1980**, *1*, 163–175.

[8] A. G. Jolley, D. D. Taylor, N. J. Schreiber, E. D. Wachsman, *J. Am. Ceram. Soc.* **2015**, *98*, 2902–2907.

[9] A. Jalalian-Khakshour, C. O. Phillips, L. Jackson, T. O. Dunlop, S. Margadonna, D. Deganello, *J. Mater. Sci.* **2020**, *55*, 2291–2302.

[10] J. Yang, G. Liu, M. Avdeev, H. Wan, F. Han, L. Shen, Z. Zou, S. Shi, Y.-S. Hu, C. Wang, X. Yao, *ACS Energy Lett.* **2020**, *5*, 2835–2841.

[11] A. Clearfield, M. A. Subramanian, W. Wang, P. Jerus, *Solid State Ionics* **1983**, *9–10*, 895–902.

[12] J. P. Boilot, J. P. Salanié, G. Desplanches, D. Le Potier, *Mater. Res. Bull.* **1979**, *14*, 1469–1477.

[13] J. S. Lee, C. M. Chang, Y. l. Lee, J. H. Lee, S. H. Hong, *J. Am. Ceram. Soc.* **2004**, *87*, 305–7.

[14] S. Naqash, Ph.D. thesis, **2018**, https://publications.rwth-aachen.de/record/754543/.

[15] N. G. Bukun, E. I. Moskvina, *Solid State Ionics* **1996**, *86–88*, 107–111.

[16] D. H. Aguilar, L. C. Torres-Gonzalez, L. M. Torres-Martinez, T. Lopez, P. Quintana, *J. Solid State Chem.* **2001**, *158*, 349–357.

[17] Y. Kim, H. Kim, S. Park, I. Seo, Y. Kim, *Electrochim. Acta* **2016**, *191*, 1–7.

[18] A. Tiliakos, M. Iordache, A. Marinoiu, *Appl. Sci.* **2021**, *11*, 8432.

[19] F. Tietz, *AIMS Mater. Sci.* **2017**, *4*, 1305–1318.

[20] U. Warhus, J. Maier, A. Rabenau, *J. Solid State Chem.* **1988**, *72*, 113–125.

[21] T. Feist, P. K. Davies, E. Vogel, *Thermochim. Acta* **1986**, *106*, 57–61.

[22] D. O. Savinykh, S. A. Khainakov, A. I. Orlova, S. Garcia-Granda, *Russ. J. Inorg. Chem.* **2018**, *63*, 714–724.

[23] M. Barj, G. Lucazeau, C. Delmas, *J. Solid State Chem.* **1992**, *100*, 141–150.

[24] G. Collin, R. Comes, J. P. Boilot, P. Colomban, *J. Phys. Chem. Solids* **1986**, *47*, 843–854.

[25] M. Giarola, A. Sanson, F. Tietz, S. Pristat, E. Dashjav, D. Rettenwander, G. J. Redhammer, G. Mariotto, *J. Phys. Chem. C* **2017**, *121*, 3697–3706.

[26] G. Greczynski, L. Hultman, *Sci. Rep.* **2021**, *11*, 11195.

[27] S. Wang, H. Xu, W. Li, A. Dolocan, A. Manthiram, *J. Am. Chem. Soc.* **2018**, *140*, 250–257.

[28] P. J. Squattrito, P. R. Rudolf, P. G. Hinson, A. Clearfield, K. Volin, J. D. Jorgensen, *Solid State Ionics* **1988**, *31*, 31–40.

[29] Z. Azdad, L. Marot, L. Moser, R. Steiner, E. Meyer, *Sci. Rep.* **2018**, *8*, 16251.

[30] S. Naqash, D. Sebold, F. Tietz, O. Guillon, *J. Am. Ceram. Soc.* **2019**, *102*, 1057–1070.

[31] A. G. Jolley, G. Cohn, G. T. Hitz, E. D. Wachsman, *Ionics* **2015**, *21*, 3031–3038.

[32] A. Hayashi, K. Noi, N. Tanibata, M. Nagao, M Tatsumisago, *J. Power Sources* **2014**, *258*, 420–423.

[33] S Narayanan, S. Reid, S. Butler, V. Thangadurai, *Solid State Ionics* **2019**, *331*, 22–9.

[34] S. M. Lee, S. T. Lee, D. H. Lee, S. H. Lee, S. S. Han, S. K. Lim, *J. Ceram. Process Res.* **2015**, *16*, 49–53.

[35] Y. Lu, C. Z. Zhao, H. Yuan, X. B. Cheng, J. Q. Huang, Q. Zhang, *Adv. Funct. Mater.* **2021**, *31*, 2009925.

[36] Q. Ma, T. Ortmann, A. Yang, D. Sebold, S. Burkhardt, M Rohnke, F. Tietz, D. Fattakhova-Rohlfing, J. Janek, O. Guillon, *Adv. Energy Mater.* **2022**, *12*, 2270164.

[37] W. Zhou, Y. Li, S. Xin, J. B. Goodenough, *ACS Cent. Sci.* **2017**, *3*, 52–57.

[38] Q. Ma, C. L. Tsai, X. K. Wei, M. Heggen, F. Tietz, J. T. S. Irvine, *J. Mater. Chem. A* **2019**, *7*, 7766–7776.

[39] E. Querel, I. Seymour, A. Cavallaro, Q. Ma, F. Tietz, A. Aguadero, *J. Phys. Energy* **2021**, *3*, 044007, https://iopscience.iop.org/article/10.1088/2515-7655/ac2fb3.

[40] T. Lan, C. L. Tsai, F. Tietz, X. K. Wei, M. Heggen, R. E. Dunin-Borkowski, *Nano Energy* **2019**, *65*, 104040.

[41] S. Burkhardt, M. Rohnke, T. Ma, G.-L. Xu, Y. Li, B. Song, X. Zeng, C.-C. Su, W. L. Mattis, F. Guo, Y. Ren, R. Kou, C. Sun, S. M. Heald, H.-H. Wang, R. Shahbazian-Yassar, J. Jorne, Z. Chen, K. Amine, *ACS Appl. Energ. Mater.* **2018**, *1*, 5735–5745.

[42] T. Roisnel, J. Rodríguez-Carvajal, *Mater. Sci. Forum* **2001**, *378–381*, 118–123.

RESEARCH ARTICLE

The study investigates the efficiency of high energy milling (HEM) in simplifying the processing of Sodium NASICON solid electrolyte, optimised the method and studied the stability of the HEM SE against Na metal and NMO active material.

A.'u I. Gebi, Dr. O. Dolokto, L. Mereacre, U. Geckle, Dr. H. Radinger, Dr. M. Knapp, Prof. H. Ehrenberg*

Characterization and Comparative Study of Energy Efficient Mechanochemically Induced NASICON Sodium Solid Electrolyte Synthesis